FreMIM: Fourier Transform Meets Masked Image Modeling
for Medical Image Segmentation

Wenxuan Wang[1,*]   Jing Wang[1,*]   Chen Chen[2]   Jianbo Jiao[3]
Yuanxiu Cai[1]   Shanshan Song[1]   Jiangyun Li[1†]

[1]School of Automation and Electrical Engineering, University of Science and Technology Beijing
[2]Center for Research in Computer Vision, University of Central Florida
[3]School of Computer Science, University of Birmingham

s20200579@xs.ustb.edu.cn, chen.chen@crcv.ucf.edu, leejy@ustb.edu.cn

Abstract

The research community has witnessed the powerful potential of self-supervised Masked Image Modeling (MIM), which enables the models capable of learning visual representation from unlabeled data. In this paper, to incorporate both the crucial global structural information and local details for dense prediction tasks, we alter the perspective to the frequency domain and present a new MIM-based framework named FreMIM for self-supervised pre-training to better accomplish medical image segmentation tasks. Based on the observations that the detailed structural information mainly lies in the high-frequency components and the high-level semantics are abundant in the low-frequency counterparts, we further incorporate multi-stage supervision to guide the representation learning during the pre-training phase. Extensive experiments on three benchmark datasets show the superior advantage of our FreMIM over previous state-of-the-art MIM methods. Compared with various baselines trained from scratch, our FreMIM could consistently bring considerable improvements to model performance. The code and model are publicly available at https://github.com/jingw193/FreMIM.

1. Introduction

Since Masked Language Modeling (MLM) obtained great success in the field of Natural Language Processing (NLP) [18], numerous works [4,12,26,40,50,53] have transferred this idea to the vision domain, making Mask Image Modeling (MIM) an effective pre-training strategy. One of the most representative approaches is Masked Autoencoders (MAE) [26], which pre-trains the model by masking partial regions within an image and reconstructing them.

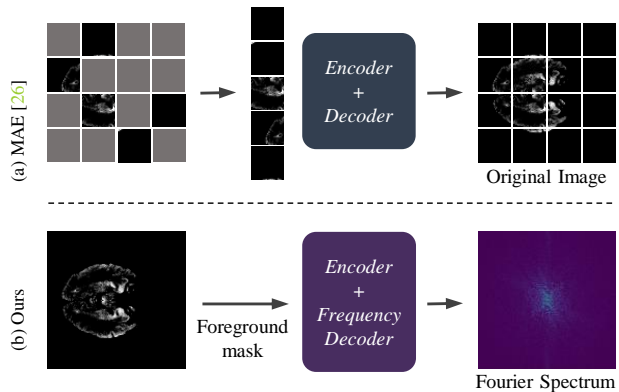*Equal Contribution.†Corresponding author.

Figure 1. The comparison of key ideas between the MAE framework and our proposed FreMIM. (a) MAE: randomly masks the patch tokens and reconstructs raw pixels of the original image. (b) Our FreMIM: randomly masks the **foreground pixels** and reconstructs the **Fourier spectrum** of the original image.

After the pre-training, the model is fine-tuned on various downstream tasks and achieves state-of-the-art (SOTA) performance. Following-up works mainly focus on improving the accuracy and efficiency by introducing new designs, such as ConvMAE [23] and Siamese Image Modeling [45].

Some recent works applied MAE-based methods for medical image analysis [27, 44, 54] and achieved promising results across various benchmark datasets with different modalities, including computed tomography (CT) [37] images, magnetic resonance imaging (MRI) [28], to name a few. Despite making methodological advancements and structural innovations, these methods have not essentially solved the key limitations of MAE. Although compared with other self-supervised learning (SSL) frameworks MAE can consistently help the model extract generally useful features even with few training samples (as proven by [31]), to some extent, MAE solely takes raw pixels as reconstruction targets mainly depending on local feature representation rather than fully utilizing the global information. Be-
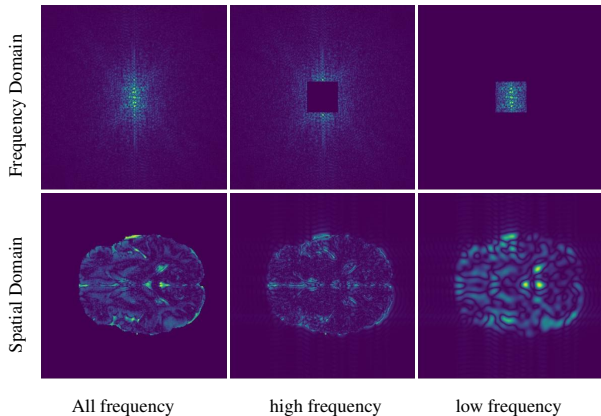
Figure 2. The visualization of the whole Fourier spectrum, high-frequency components, and low-frequency counterparts respectively, the high/low-frequency components of which are acquired by applying the corresponding high/low-pass filters on the whole Fourier spectrum. As illustrated in the second row of the figure, the inspiration for our FreMIM comes from the observations that local details (like texture and contours) mainly lie in the high-frequency components while the global and smooth structural information is rich in the low-frequency counterparts.

sides, since the model is expected to possess the ability to extract features with multiple semantic levels at different stages, only the output from the last stage is fed into the decoder for the reconstruction task, lacking the supervision from other stages to provide multi-scale information. In summary, previous works [4, 26, 49] crucially require a certain trade-off between the local details and contextual semantics, which leaves room for further improvement. Furthermore, due to high acquisition costs and patients' privacy, the training samples of commonly small-scale medical datasets are relatively limited, but none of these previous works have taken this unique characteristic of medical image datasets into consideration and made tailored designs.

Therefore, in order to fully exploit the potential of MIM-based methods for medical image segmentation under the circumstance of limited training samples, *how to acquire the global information while preserving the detailed local features as much as possible* has become the key problem. Considering the nature of Fourier Transform in image processing, it might be a possible solution. As studied in lots of previous works [5, 7, 14, 30, 43] and shown in Fig. 2, the detailed texture information mainly lies in the high-frequency components and the low-frequency counterparts carry rich global information. Following this observation, an intuitive solution would be exploring the powerful potential of MIM coupled with Fourier Transform.

To this end, aiming at the joint modeling of both local and global features during SSL pre-training, we propose a new MIM-based framework conducted in the Fourier domain, namely *FreMIM*, which to our knowledge is the first work to explore the potential of MIM with Fourier Trans-

form for 2D medical image segmentation. Specifically, our FreMIM first masks out a portion of randomly selected image pixels and then predicts the corresponding missing frequency spectrum of the input image in the Fourier domain. Since medical images of the same organ essentially correspond to similar features, we conduct difficult cross-domain reconstruction tasks to avoid learning with shortcuts and achieve strong representation capability. Meanwhile, inspired by previous findings [47] that the detailed structural information mainly lies in the high-frequency components and the high-level semantics are abundant in the low-frequency counterparts, the proposed bilateral aggregation decoder is leveraged to sequentially apply the Fourier Transform on the original image and employ low/high-pass filters on the converted Fourier spectrum to get the expected reconstruction target. Such a multi-stage supervision approach could better guide the model pre-training, resulting in better representations for segmentation. Besides, we propose an effective foreground masking strategy as the alternative to the original random masking, which is proven to be more suitable for textures and details modeling for medical image segmentation. In summary, the main contributions of this work are summarized as follows:

- We present the first study on exploring the powerful potential of masked image modeling with frequency domain for medical image segmentation tasks. The proposed FreMIM is a generic self-supervised pre-training framework that can be integrated with different model architectures (*i.e.* both CNNs and Transformers).
- By designing a multi-stage supervision scheme coupled with a well-designed bilateral aggregation decoder, we propose a new cross-domain masking-reconstruction framework for masked image modeling paradigm.
- A simple yet effective masking strategy among foreground pixels is proposed as a better alternative to the original random masking pixels strategy, providing more precise and informative masks for the following self-supervised representation learning.
- Without introducing any extra training samples, extensive experiments on three benchmark datasets and three representative 2D baselines validate the effectiveness of the proposed FreMIM, outperforming other previous alternative self-supervised state-of-the-art approaches.

2. Related Work

2.1. Masked Image Modeling

As a powerful self-supervised learning paradigm, MIM has attracted increasing community interest recently. By reconstructing the masked portion of images, models could learn informative feature representations that are favorable for various visual downstream tasks.

On Natural Images. Previous works of reconstruction tar-

gets could be divided into three categories, including discrete tokens [4, 40], feature maps [49, 53], and raw image pixels [26, 50]. For example, BEiT [4] and BEiTV2 [40] added a classifier to predict masked visual tokens, and it is supervised by the encoded image patches from offline tokenizer. Inspired by the self-distillation paradigm in DINO [9], iBOT [53] adopted a teacher-student framework to perform MIM. The teacher network serves as an online tokenizer to learn visual semantics from all image patches, while the student network only processes visible patches. Moreover, MaskFeat [49] first explored features as prediction targets. Besides, SimMIM [50] discarded the tokenizer and patch classification, simply employing RGB values of raw pixels as predicted targets. Without feeding masked tokens into the encoder, MAE [26] designed a simple decoder to reconstruct image patches, leading to a considerable reduction of computation complexity during pre-training.

On Medical Images. At the same time, various works [24, 27, 44, 51, 52, 54] have explored the effectiveness of MIM pre-training on various medical benchmark datasets. Zhou et al. [54] applied MAE pre-training paradigm for medical image segmentation and significantly improved the results. Huang et al. [27] proposed a manually settled attentive reconstruction loss that pays more attention to the informative regions. Tang et al. [44] explored the hierarchical structure for full extraction of image features and constructed a self-supervised pre-training framework with three proxy tasks. However, the random masking strategy of patches utilized previously is rough and may result in computation waste on the useless background. Considering that informative foreground and useless background are discriminated in medical images, we design a masking strategy among foreground pixels to obtain more effective masks, assisting models in better representation learning. Moreover, our method could cast off the reliance of the pre-training paradigm on specific model structures and consistently boost model performance, which is different from previous works (*e.g.* Swin Transformer and CNN-based models can not be directly integrated with MAE).

2.2. Fourier Transform

Recently, a series of research [29, 41, 55] have performed Fourier Transform on images and leveraged the frequency information to improve model performance and efficiency. For example, [41] utilized Fast Fourier Transform (FFT) as the alternative to self-attention modules in the original Transformer, successfully acquiring global information with low computation costs. [29] designed a novel focal frequency loss for Fourier spectrum supervision to improve popular image generative model performance.

Inspired by these previous researches [5, 7, 14, 30, 43], we randomly mask the original image and reconstruct the Fourier spectrum in the frequency domain to help the model learn more generalized global representation in a cross-domain masking-reconstruction manner. In addition, multi-stage supervision coupled with leveraged specific characteristics of FFT (*i.e.* high-pass and low-pass frequency components) is also proposed to better guide the model representation learning among different stages.

3. Methodology

3.1. Preliminary: Fourier Transform

Since Discrete Fourier Transform (DFT) plays a vital role in our proposed method, we first give a brief review of the 2D DFT that serves as an indispensable technique for traditional signal analysis. Given a 2D signal $\mathbf{F} \in \mathbb{R}^{W \times H}$, its corresponding 2D-DFT can be defined as:

$$f(u, v) = \sum_{h=0}^{H-1} \sum_{w=0}^{W-1} F(h, w) e^{-j2\pi \left(\frac{uh}{H} + \frac{vw}{W} \right)}, \qquad (1)$$

where $F(h, w)$ represents the signal located at (h, w) in $\mathbf{F}$, while the u and v are indices of horizontal and vertical spatial frequencies in the Fourier spectrum. Correspondingly, the 2D Inverse DFT (2D-IDFT) is formulated as:

$$F(h, w) = \frac{1}{HW} \sum_{u=0}^{H-1} \sum_{v=0}^{W-1} f(u, v) e^{j2\pi \left(\frac{uh}{H} + \frac{vw}{W} \right)}. \qquad (2)$$

Both DFT and IDFT can be accelerated with their fast version, FFT algorithm [38]. For medical images with various modalities, the Fourier Transform is operated on each channel independently. Besides, as already shown in previous works [5, 7, 14, 30, 43], the detailed structural texture information of an image mainly lies in the high-frequency part of the Fourier spectrum while the global information is rich in the low-frequency counterpart. Fig. 2 presents the visualization of this intriguing characteristic.

3.2. The Proposed FreMIM

Overall Architecture. An overview of the proposed SSL framework namely FreMIM is presented in Fig. 3. Given an input medical image slice $X \in \mathbb{R}^{C \times H \times W}$ with a spatial resolution of $H \times W$ and C channels (# of modalities), the proposed foreground masking strategy is first employed on the original image to generate the masked image. Then, the generic encoder (*i.e.* according to various pre-training requirements, **both CNNs and Transformers encoder can be easily integrated into our framework**) takes the masked image as input, capturing the masked visual features through the hierarchical structure. After that, the encoded feature representations at different stages are jointly fed into our well-designed bilateral aggregation decoder, gradually producing the reconstructed Fourier spectrum with both low-level detail information and high-level semantic representation. By sequentially applying Fourier
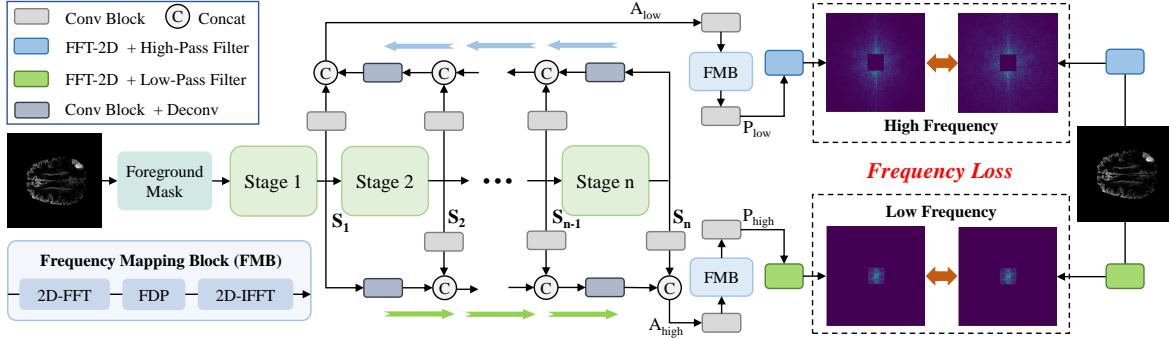
Figure 3. The overall architecture of our proposed FreMIM. At first, the input medical image is corrupted by the foreground masking strategy and then fed into the encoder, which consists of several stages with a hierarchical structure. The captured feature maps at different stages (*i.e.* S_1, S_2, ... S_n) are fused by a bilateral aggregation decoder to generate the aggregated high-level and low-level feature representations (*i.e.* A_{high} and A_{low}). For the fused feature of each semantic level, an FMB is applied respectively to learn its recessive information in the frequency domain, resulting in the acquired P_{low} and P_{high}. Finally, the low-pass and high-pass Fourier spectra are both adopted as the reconstruction target to better guide the model to capture local details and global information.

Transform on the original image and employing low/high-pass filters on the converted Fourier spectrum to acquire the expected reconstruction target, the reconstruction loss is applied to the similarity between the reconstructed spectrum and the expected low/high-pass spectrum target, realizing the helpful multi-stage supervision scheme with both low- and high-level representations in an end-to-end manner.

Masking Strategy. As experimentally illustrated in several previous works [4, 23, 26, 40, 45, 50], random masking strategy is not only simple but also effective for MIM-based self-supervised learning paradigm on large-scale natural images. However, different from natural images, the distribution of foreground and background pixels in medical images is extremely unbalanced. So randomly selecting spatial positions of a medical image would inevitably cause the generated mask to mostly cover background pixels and too many foreground pixels of the objects are reserved, counting against the model's reconstruction ability. To this end, we propose a simple yet effective foreground masking strategy to address this uneven distribution issue.

Specifically, given a binary mask $M \in \{0, 1\}^{H \times W}$ initialized with zeros, its value at each spatial position is determined by whether the corresponding pixel value belongs to the foreground or not. If a pixel belongs to the foreground area, it will be filtered as one of the candidates to be masked during self-supervised pre-training. Since a medical image commonly consists of diverse channels, each one emphasizing a different foreground area, we take their overlapping parts as the final masked regions. The overall foreground masking strategy can be defined as:

$$M_n(x, y) = \begin{cases} 0, & P_n(x, y) = 0 \\ 1, & P_n(x, y) \neq 0 \end{cases}, \qquad (3)$$

$$\mathcal{M} = M_1 \cap M_2 \cap M_3 ... \cap M_n, \qquad (4)$$

$$X_{\mathcal{M}} = \mathcal{M} \odot X, \qquad (5)$$

where $\odot$ is the Hadamard product, $P_n(x, y)$ represents the specific pixel value of the corresponding position (x, y), M_n denotes the generated mask of the specific image modality M_n. $\mathcal{M}$ and $X_{\mathcal{M}}$ respectively indicate the final mask of the original image and the masked image that will be fed into the model for the following reconstruction task.

Generic Encoder. As for the selection of encoder in our framework, FreMIM is not restricted to any specific kind of structure thanks to our pixel-wise foreground masking strategy. Dislike some previous MIM-based methods can only be incorporated with various Vision Transformers (*e.g.* Due to the random masking strategy of embedded image patches, MAE is only applicable for ViT [19] without the consideration of CNNs or hierarchical Transformer architecture), our FreMIM is a generic and flexible framework, which means both CNN-based and Transformer-based models can be easily integrated with our FreMIM for effective self-supervised pre-training. Taking the aforementioned masked image as input, the network encoder gradually encodes the masked image slice with the hierarchical structure, producing the feature representations with diverse levels (*i.e.* from low-level detail information to high-level semantics). In this paper, three previous SOTA methods for medical image segmentation, *i.e.* the representatives of the CNN-Transformer hybrid architectures and Vision Transformers, are selected as the backbones to validate the effectiveness of our method (more details are in Sec. 4).

Multi-stage Supervision Scheme. Both low-level details and high-level global semantics are crucial, especially for medical image segmentation. The expectation of an effective SSL paradigm is to guide the visual backbone to learn the required representations with different levels through the hierarchical structure. Following this intuition, we propose to design a multi-stage supervision scheme to fully supervise the representation learning of hierarchical stages.

As emphasized in Sec. 1, high-level and low-level in-

formation of an image is distributed in different frequency bands of the Fourier spectrum. So we propose to separately take advantage of the low-pass and high-pass Fourier spectrum as the supervision signal (*i.e.* **reconstruction target**). One of the most intuitive ways is to utilize the identical high-pass Fourier spectrum to directly supervise multiple low-level stages and vice versa for low-pass counterparts. However, there are mainly two drawbacks for this intuitive manner. On the one hand, this manner is kind of unreasonable and it violates the original intention of model learning at various low-level stages cause the feature representations learned at different low-level stages should be naturally different instead of the same. On the other hand, such a supervision method is too direct and simple, and does not make full use of the correlation between the captured multi-stage features by the hierarchical structure to help the model better perform the MIM pretext task.

With regard to this, a well-designed **bilateral aggregation decoder** is proposed to better solve the reconstruction task in the frequency domain, further helping the encoder to learn a more generalized and more meaningful feature representation. Specifically, inside the proposed bilateral aggregation decoder, the encoded features at different stages are converged to the lowest stage (*i.e.* with maximum spatial resolution) and the highest stage (*i.e.* with minimum spatial resolution) in a bottom-up and top-down manner, respectively. In other words, the BAD separately aggregates the feature maps of different stages into the lowest and highest resolution. Specifically, for ViT, the feature maps of layers 4th, 8th, and 12th are upsampled by 8, 4, and 2 times respectively to be fed to the BAD, following the deconvolution module in UNETR. To be clear, the captured features of each adjacent stage will be fed into the convolutional block to achieve the strict alignment of both spatial resolution and channel dimension, which can be expressed as:

$$\mathbf{A}_{\text{low}} = \mathbf{Cat}(\mathbf{C}(S_1), \mathbf{Dc}(..., \mathbf{Cat}(\mathbf{C}(S_{n-1}), \mathbf{Dc}(S_n)))), \quad (6)$$
$$\mathbf{A}_{\text{high}} = \mathbf{Cat}(\mathbf{C}(S_n), \mathbf{Dc}(..., \mathbf{Cat}(\mathbf{C}(S_2), \mathbf{Dc}(S_1)))), \quad (7)$$

where $\mathbf{A}_{\text{high}}$ and $\mathbf{A}_{\text{low}}$ separately denote the bilaterally aggregated high-level and low-level feature representations, $\mathbf{C}$, $\mathbf{Dc}$ and $\mathbf{Cat}$ indicate the convolutional block, deconvolution block, and concatenation operation respectively, S_i denotes the feature maps output by the stage i.

Then, the aggregated feature representations at the lowest stage and highest stage will be mapped to the frequency domain through the introduced frequency mapping block (as illustrated in Fig. 3), which are followed by the low-pass and high-pass filters to get the corresponding high-pass and low-pass prediction spectrum for the employed reconstruction loss. Specifically, the frequency mapping block (FMB) consists of a 2D-DFT, a Frequency Domain Perceptron (FDP), and a 2D-IDFT, which can be calculated as:

$$\mathbf{P}_{\text{low}} = IDFT(W \odot DFT(\mathbf{A}_{\text{low}}) + b), \quad (8)$$

$$\mathbf{P}_{\text{high}} = IDFT(W \odot DFT(\mathbf{A}_{\text{high}}) + b), \quad (9)$$

where DFT and $IDFT$ represent the Fast Fourier Transform and Inverse Fast Fourier Transform. W and b are both learnable parameters, $\odot$ is the Hadamard product. In this way, a powerful SSL framework for **cross-domain reconstruction** is built with the benefit of the Fourier Transform's unique characteristics. Although such a cross-domain reconstruction task is more difficult than intra-domain reconstruction, it can also assist the model in learning more robust feature representation, which is fully demonstrated in the following experimental section.

3.3. Pre-training Strategy

Frequency Loss. To alleviate the weight imbalance between different frequency band spectrums and facilitate the reconstruction of difficult frequency bands, we adopt focal frequency loss [29] as the loss function $\mathcal{L}_{\text{freq}}$ to implement gradient updating of weights for both low and high-frequency mapping, which is defined as:

$$\mathcal{L}_{\text{freq}} = \frac{1}{HW} \sum_{u=0}^{H-1} \sum_{v=0}^{W-1} \omega(u,v) \odot \gamma(f(u,v), \hat{f}(u,v))^2, \quad (10)$$

where $f(u,v)$ is the predicted 2D-DFT of spatial frequency coordinate (u,v) while $\hat{f}(u,v)$ denotes its corresponding Ground Truth value. $\gamma(f, \hat{f})$ calculates the squared Euclidean distance between actual and predicted values as their frequency distance. And ω is the spectrum weight matrix of a given location, which suppresses weights of easy frequencies. The calculation formulas are as follows:

$$\omega(u,v) = \gamma(f(u,v), \hat{f}(u,v))^\beta, \quad (11)$$

$$\gamma(f, \hat{f}) = \sqrt{(\mathcal{R} - \tilde{\mathcal{R}})^2 + (\mathcal{I} - \tilde{\mathcal{I}})^2}, \quad (12)$$

where β is a scaling factor for flexibility (β=1 by default) .

Overall Loss. During pre-training, our FreMIM learns representation by solving content gestalt from both high-pass and low-pass frequency:

$$\mathcal{L} = \mathcal{L}_{\text{freq}}(\mathbf{F}_H(\mathbf{P}_{\text{low}}), \mathbf{F}_H(\mathbf{T})) \quad (13)$$
$$+ \alpha \mathcal{L}_{\text{freq}}(\mathbf{F}_L(\mathbf{P}_{\text{high}}), \mathbf{F}_L(\mathbf{T})),$$

where $\mathbf{F}_H$ and $\mathbf{F}_L$ represent high-pass and low-pass frequency filter respectively. $\mathbf{T}$ indicates the original images. As shown in Fig. 3, $\mathbf{P}_{\text{low}}$ is obtained by highest-stage and $\mathbf{P}_{\text{high}}$ is the opposite. α is the weight of high-level semantic information branches (α = 3 by default).

4. Experiments and Results

In this section, *focusing on solely exploiting the given training samples (*i.e.* the pre-training data only includes the*

Table 1. Comparison with previous self-supervised learning frameworks. '-' represents training from scratch. Without introducing any extra samples, our FreMIM can consistently boost the model performance by a large margin compared with randomly initialized baselines.

Baseline	Backbone	Pre-train Method	Dice Score (%) ↑			
			ET	WT	TC	Average
TransBTSV2 [32]	CNN-Transformer	-	77.11	90.32	82.90	83.44
TransBTSV2 [32]	CNN-Transformer	FreMIM	**79.65 (+2.54)**	**90.80 (+0.48)**	**83.33 (+0.43)**	**84.59 (+1.15)**
UNETR [25]	ViT-B/16 [20]	-	75.28	88.42	76.33	80.01
UNETR [25]	ViT-B/16 [20]	MAE [26]	75.18 (-0.10)	88.95 (+0.53)	78.47 (+2.14)	80.87 (+0.86)
UNETR [25]	ViT-B/16 [20]	DINO [9]	75.22 (-0.06)	88.33 (-0.09)	75.89 (-0.44)	79.81 (-0.20)
UNETR [25]	ViT-B/16 [20]	FreMIM	**76.50 (+1.22)**	88.86 (+0.44)	**78.82 (+2.49)**	**81.39 (+1.38)**
Swin UNETR [44]	Swin-B [34]	-	76.68	89.89	79.98	82.18
Swin UNETR [44]	Swin-B [34]	SimMIM [50]	77.59 (+0.91)	**90.47 (+0.58)**	80.34 (+0.36)	82.80 (+0.62)
Swin UNETR [44]	Swin-B [34]	Swin UNETR [44]	77.85 (+1.17)	89.63 (-0.26)	78.65 (-1.33)	82.04 (-0.14)
Swin UNETR [44]	Swin-B [34]	FreMIM	**78.38 (+1.70)**	90.06 (+0.17)	**81.05 (+1.07)**	**83.16 (+0.98)**

specific downstream datasets without introducing any extra data) for 2D medical image segmentation (e.g. solely BraTS 2019 is used for pre-training when evaluating brain tumor segmentation), extensive experiments on three benchmark datasets are conducted to fully verify the effectiveness of FreMIM. Note that the numbers between parenthesis represent the gains with respect to specific baselines trained from scratch, while the red and blue color denote accuracy increase and decrease respectively. To save space, the visual comparisons in terms of segmentation and reconstruction results are presented in supplementary material.

4.1. Experimental Setup

Data and Evaluation Metrics. Our proposed method is evaluated on three benchmark datasets (*i.e.* BraTS 2019 [2, 3, 35], ISIC 2018 [16, 46] and ACDC 2017 [6]) for medical segmentation. Due to space limit, more detailed elaborations are presented in the supplementary material.

Implementation Details. The specific implementation details can be found in the supplementary material.

4.2. Results and Analysis

Comparison with Previous SSL Frameworks. Based on five-fold cross-validation on the BraTS 2019 training set, we perform a fair comparison between our proposed FreMIM and previous self-supervised learning methods on various baselines including TransBTSV2 [32], UNETR [25], and Swin UNETR [44], demonstrating the effectiveness and generalization capability of our FreMIM. For comprehensive comparisons, we select multiple self-supervised learning methods (*i.e.* MAE [26], SimMIM [50], DINO [9] and Swin UNETR [44]), among which MAE and SimMIM have achieved promising results on natural images, DINO is a representative contrastive learning method, and Swin UNETR is a representative of the previous efforts on SSL methods for medical image analysis. *To be clear, since some of these previous methods are limited to backbone structures (e.g. MAE cannot be adapted to Swin Transformer backbone due to the token-dropping operation), for other meth-*

ods we kept their original backbone as in their papers to achieve a fair comparison, which implicitly demonstrates our method's superior versatility to various backbones.

As presented in Table 1, our FreMIM shows great superiority over all three baselines. Compared to training from scratch, the Average Dice scores on three baselines are simultaneously increased by 1.14%, 1.38%, and 0.98% respectively after pre-training with our framework. In comparison with MAE on UNETR and SimMIM on Swin UNETR, our FreMIM greatly improves model performance with the benefit of exploiting MIM in the frequency domain for global representation learning. Since contrastive learning methods mainly focus on learning high-level semantics by instance discrimination task, neglecting the fine-grained representation learning results in poor results for UNETR with DINO pre-training. In contrast, FreMIM takes advantage of the smooth structure information of organs and detailed contours and textures as supervision signals, better guiding the model's high-level and low-level representation learning. Additionally, the Swin UNETR pre-training method achieves inferior performance. We believe the reasonable explanation for this phenomenon is that the Swin UNETR pre-training method heavily relies on the number of training samples to acquire useful prior knowledge (*i.e.* it can not help models to capture the helpful representations as expected under the circumstance of limited pre-training samples). On the contrary, without introducing any extra samples, our FreMIM can greatly boost model performance compared with random initialization, suggesting the effectiveness and data-efficient characteristic of our method. In summary, our FreMIM with the advantages of the frequency domain is a generic and powerful MIM-based framework, which could bring consistent improvement in model performance without introducing extra data.

Evaluation on Brain Tumor Segmentation. Comparative experiments are also conducted on the BraTS 2019 validation set. As shown in Table 2 (a), our FreMIM achieves superior performance than previous methods with the competitive Dice scores of 79.74%, 90.23%, and 81.25% on ET,

Table 2. Performance comparisons on BraTS 2019, ISIC 2018 and ACDC 2017 datasets. Here TransBTSV2 denotes the 2D version of the original model to fit our proposed SSL framework.

(a) BraTS 2019

Method	Dice Score (%) ↑			Hausdorff Dist. (mm) ↓		
	ET	WT	TC	ET	WT	TC
3D U-Net [15]	70.86	87.38	72.48	5.062	9.432	8.719
V-Net [36]	73.89	88.73	76.56	6.131	6.256	8.705
Attention U-Net [39]	75.96	88.81	77.20	5.202	7.756	8.258
Chen et al. [13]	74.16	**90.26**	79.25	4.575	**4.378**	7.954
Li et al. [33]	77.10	88.60	81.30	6.033	6.232	7.409
Frey et al. [22]	78.70	89.60	80.00	6.005	8.171	8.241
TransBTS [48]	78.36	88.89	**81.41**	5.908	7.599	7.584
TransUNet [10]	78.17	89.48	78.91	4.832	6.667	7.365
Swin-UNet [8]	78.49	89.38	78.75	6.925	7.505	9.260
TransBTSV2 [32]	78.63	90.09	80.23	3.729	6.194	7.725
TransBTSV2	**79.74**	90.23	81.25	**3.209**	5.875	**6.934**
+FreMIM	**+1.11**	**+0.14**	**+1.02**	**-0.520**	**-0.319**	**-0.791**

(b) ISIC 2018

Method	JI	Dice	Accuracy	Recall	Precision
U-Net [42]	81.69	88.81	95.68	88.58	91.31
U-Net++ [56]	81.87	88.93	95.68	89.10	90.98
AttU-Net [39]	81.99	89.03	95.77	88.98	91.26
DeepLabv3+ [11]	82.32	89.26	95.87	89.74	90.87
CPF-Net [21]	82.92	89.63	96.02	**90.62**	90.71
BCDU-Net [1]	80.84	88.33	95.48	89.12	89.68
Ms RED [17]	83.45	89.99	96.19	90.49	91.47
TransBTSV2 [32]	81.96	92.56	95.88	90.21	90.78
TransBTSV2	**83.53**	**93.39**	**96.44**	90.18	**92.61**
+FreMIM	**+1.57**	**+0.83**	**+0.56**	-0.03	**+1.83**

(c) ACDC 2017

Method	RV	Myo	LV	Average
U-Net [42]	86.91	87.17	90.65	88.25
AttU-Net [39]	86.78	86.93	91.84	88.52
Swin-UNet [8]	86.62	88.72	92.44	89.26
TransUNet [10]	87.04	88.51	**92.85**	89.47
TransBTSV2 [32]	86.80	87.76	91.87	88.81
TransBTSV2 [32]	**87.12**	**88.87**	92.69	**89.56**
+FreMIM	**+0.32**	**+1.11**	**+0.82**	**+0.75**

Table 3. Ablation study on the reconstruction target and supervision scheme.

low-level target	high-level target	Dice Score (%) ↑			
		ET	WT	TC	Average
-	-	77.11	90.32	82.90	83.44
high-pass	-	77.82	90.60	**83.60**	84.01(+0.57)
-	low-pass	77.44	90.12	82.89	83.48(+0.04)
original image	original image	79.33	90.23	81.95	83.83(+0.39)
all frequency	all frequency	79.12	**90.80**	82.58	84.17(+0.73)
low-pass	high-pass	79.01	90.41	83.00	84.14(+0.70)
high-pass	low-pass	**79.65**	**90.80**	83.33	**84.59(+1.15)**

strong capability on skin lesion segmentation.

Evaluation on Cardiac Segmentation. To evaluate the generalization ability of our proposed FreMIM, we also conduct experiments of cardiac segmentation on MRI scans utilizing the ACDC 2017 dataset [6]. Since the official evaluation is supported by the online evaluation platform, the five-fold cross-validation is performed on ACDC 2017 training set. The quantitative results on ACDC 2017 training set are presented in Table 2 (c). By guiding the baseline to better capture both the crucial high-level semantics and local detailed information, it is obvious that with boosted model performance in comparison with the baseline, our framework once again achieves comparable or even higher Dice scores than previous SOTA methods.

4.3. Ablation Studies

We conduct extensive experiments to prove the effectiveness of our FreMIM and validate its design rationale based on 5-fold cross-validation on BraTS 2019 training set, while TransBTSV2 [32] is selected as baseline for ablation study.

Reconstruction Target and Supervision Scheme. Firstly, we explore the effect of different types of reconstruction targets and verify the effectiveness of our introduced multi-stage supervision scheme. The quantitative results are presented in Table 3. In comparison with random initialization in the first row, introducing either high-pass Fourier spectrum or low-pass counterpart as the reconstruction target at the corresponding low-level or high-level stage both lead to better segmentation performance to some extent. On the basis of this kind of single-level supervision manner, we further explore the effectiveness of a multi-level supervision scheme. As can be clearly seen in Table 3 below the dividing line, simultaneously taking advantage of high-pass and low-pass frequency components, that carry abundant local details and global structural information, results in the best segmentation accuracy with the highest Average Dice Score of 84.59%, fully demonstrating the powerful potential and rationale design of our FreMIM. No matter whether the reconstruction target is adjusted to the original image, the whole Fourier spectrum, or exchanged low/high-level target, it will all lead to a considerable decrease in model performance,

WT, and TC respectively. In addition, it is notable that our method realizes a considerable decrease of Hausdorff distance on TC, reaching $6.934mm$. Without introducing any extra training samples, the proposed FreMIM can greatly boost model performance and outperform other previous SOTA approaches. The considerable improvements made by FreMIM are powerful evidence of the effectiveness of using our method on MRI benchmarks.

Evaluation on Skin Lesion Segmentation. We also verified the generality of FreMIM on RGB images dataset namely ISIC 2018 compared with the other seven well-performed algorithms. It could be seen from Table 2 (b) that, with the informative feature representations obtained from pre-training stages, our method could reach great performance on ISIC 2018 the five-fold cross-validation. Specifically, compared with previous SOTA methods, our results are higher on both JI, Dice, Accuracy, and Precision metrics. It is worth noting that our method promotes **1.57%** and **1.83%** on Dice score and Precision compared to training from scratch, demonstrating that FreMIM also presents

which once again proves the strong theoretical rationale of exploiting FFT with the proposed FreMIM.

Table 4. Ablation study on the masking strategy.

Masking strategy	Dice Score (%) ↑			
	ET	WT	TC	Average
baseline	77.11	90.32	82.90	83.44
random mask	79.07	90.64	83.19	84.30(+0.86)
block wise mask	79.03	90.00	82.11	83.71(+0.27)
foreground mask	**79.65**	**90.80**	**83.33**	**84.59(+1.15)**

Masking Strategy. Then we investigate the influence of different masking strategies to prove the effectiveness of the proposed foreground masking strategy. Table 4 shows the performance comparison of our FreMIM with different masking strategies. It can be seen in Table 4 that the original random masking leads to an accuracy increase ↑0.86% on the Average Dice score, which is really promising. However, by replacing vanilla random masking with our simple yet powerful foreground masking strategy, the model performance on segmentation tasks can be further boosted by a considerable margin, which shows the great superiority of selecting masked pixel candidates solely among foreground over conventional masking strategy.

Table 5. Ablation study on the masking ratio.

Masking Ratio	Dice Score (%) ↑			
	ET	WT	TC	Average
baseline	77.11	90.32	82.90	83.44
0.75	78.99	90.42	83.03	84.15(+0.71)
0.50	79.19	**90.80**	83.18	84.39(+0.95)
0.25	**79.65**	**90.80**	**83.33**	**84.59(+1.15)**
0.15	79.37	90.23	82.88	84.16(+0.72)
0.15, 0.20, 0.25	78.99	90.63	**83.33**	84.32(+0.88)
0.25, 0.50, 0.75	79.23	90.62	82.88	84.24(+0.80)

Masking Ratio. After investigating the influence of various masking strategies, we further conduct experiments to seek the optimal masking ratio for our current framework. As presented in Table 5, our FreMIM with a masking ratio of 0.25 achieves the best model performance. Once the masking ratio is either too low or too high, the reconstruction task in the frequency domain would be too easy or too hard, which may hinder the model from expected representation learning during self-supervised pre-training. Besides, trying to take a step further, we also attempt to introduce a novel dynamic masking strategy (*i.e.* the masking ratio gradually increases from the lowest to the highest during pre-training) for better guidance of the expected feature representation learning, which endows the SSL with easiest-to-hardest reconstruction level. However, none of these attempts bring further accuracy improvements. Thus, the static masking strategy with a masking ratio of 0.25 is selected as our default setting.

Choice of 2 Other Hyper-parameters. Besides, we additionally conduct ablation studies on the loss weight α and the boundary definition (*i.e.* frequency threshold) between high/low frequency, in Table 6 and Table 7, where PB denotes the specific value of frequency passband, showing the efficacy of our choice for these 2 hyper-parameters.

Table 6. Ablation study on loss weight α during pre-training.

α	Dice Score (%) ↑			
	ET	WT	TC	Average
0.5	79.34	90.11	82.16	83.87
1	77.67	90.48	81.61	83.25
3	**79.65**	**90.80**	**83.33**	**84.59**
5	78.93	90.64	82.98	84.18

Table 7. Ablation study on high-/low-frequency boundary.

PB	Dice Score (%) ↑			
	ET	WT	TC	Average
5	79.46	90.31	82.69	84.15
10	**79.65**	**90.80**	**83.33**	**84.59**
20	79.20	90.53	82.31	84.01
50	78.94	90.33	82.23	83.83

Table 8. Ablation study on the number of samples for self-supervised pre-training.

Training samples	Dice Score (%) ↑			
	ET	WT	TC	Average
baseline	77.11	90.32	82.90	83.44
0.3%(*i.e.* 1 sample)	79.05	90.60	82.51	84.05(+0.61)
10%	79.06	90.41	**83.43**	84.30(+0.86)
100%	**79.65**	**90.80**	83.33	**84.59(+1.15)**

Number of Pre-training Samples. Specifically, we further investigate the effect of different percentages of training samples used for our proposed FreMIM. The quantitative results are presented in Table 8. It is clear in Table 8 that the model performance is consistently improved with more and more employed training samples for the proposed FreMIM. Besides, it is also surprising that by solely introducing 1 sample for pre-training our FreMIM can boost the model performance by a large margin (*i.e.* ↑ 0.61% on Average Dice score) compared with the randomly initialized baseline, demonstrating that our method is a data-efficient self-supervised learning paradigm.

5. Conclusion

In this paper, we presented the first study on exploring the powerful potential of MIM with frequency domain on pre-training deep learning models for medical image segmentation tasks. We focus on 2D medical image segmentation and proposed a new framework FreMIM taking advantage of both the rich global information and local details in the Fourier spectrum. Deviating from the conventional paradigm as previous MIM methods, realizing reconstruction in the frequency domain empowers the framework with stronger representation learning capability. Besides, by fully exploiting the specific characteristics contained in different frequency bands, the multi-stage supervision scheme can greatly boost the segmentation performance. Comprehensive experiments on three benchmark datasets quantitatively and qualitatively validated the effectiveness of our FreMIM, significantly improved the segmentation performance of baselines trained from scratch and showed superiority over state-of-the-art self-supervised approaches.

References

[1] Reza Azad, Maryam Asadi-Aghbolaghi, Mahmood Fathy, and Sergio Escalera. Bi-directional convlstm u-net with densley connected convolutions. In *Proceedings of the IEEE/CVF international conference on computer vision workshops*, pages 0–0, 2019.

[2] Spyridon Bakas, Hamed Akbari, Aristeidis Sotiras, Michel Bilello, Martin Rozycki, Justin S Kirby, John B Freymann, Keyvan Farahani, and Christos Davatzikos. Advancing the cancer genome atlas glioma mri collections with expert segmentation labels and radiomic features. *Scientific data*, 4:170117, 2017.

[3] Spyridon Bakas, Mauricio Reyes, Andras Jakab, Stefan Bauer, Markus Rempfler, Alessandro Crimi, Russell Takeshi Shinohara, Christoph Berger, Sung Min Ha, Martin Rozycki, et al. Identifying the best machine learning algorithms for brain tumor segmentation, progression assessment, and overall survival prediction in the brats challenge. *arXiv preprint arXiv:1811.02629*, 2018.

[4] Hangbo Bao, Li Dong, and Furu Wei. Beit: Bert pre-training of image transformers. *arXiv preprint arXiv:2106.08254*, 2021.

[5] Moshe Bar. A cortical mechanism for triggering top-down facilitation in visual object recognition. *Journal of cognitive neuroscience*, 15(4):600–609, 2003.

[6] Olivier Bernard, Alain Lalande, Clement Zotti, Frederick Cervenansky, Xin Yang, Pheng-Ann Heng, Irem Cetin, Karim Lekadir, Oscar Camara, Miguel Angel Gonzalez Ballester, et al. Deep learning techniques for automatic mri cardiac multi-structures segmentation and diagnosis: is the problem solved? *IEEE transactions on medical imaging*, 37(11):2514–2525, 2018.

[7] Jean Bullier. Integrated model of visual processing. *Brain research reviews*, 36(2-3):96–107, 2001.

[8] Hu Cao, Yueyue Wang, Joy Chen, Dongsheng Jiang, Xiaopeng Zhang, Qi Tian, and Manning Wang. Swin-unet: Unet-like pure transformer for medical image segmentation. *arXiv preprint arXiv:2105.05537*, 2021.

[9] Mathilde Caron, Hugo Touvron, Ishan Misra, Hervé Jégou, Julien Mairal, Piotr Bojanowski, and Armand Joulin. Emerging properties in self-supervised vision transformers. In *Proceedings of the IEEE/CVF International Conference on Computer Vision*, pages 9650–9660, 2021.

[10] Jieneng Chen, Yongyi Lu, Qihang Yu, Xiangde Luo, Ehsan Adeli, Yan Wang, Le Lu, Alan L Yuille, and Yuyin Zhou. Transunet: Transformers make strong encoders for medical image segmentation. *arXiv preprint arXiv:2102.04306*, 2021.

[11] Liang-Chieh Chen, Yukun Zhu, George Papandreou, Florian Schroff, and Hartwig Adam. Encoder-decoder with atrous separable convolution for semantic image segmentation. In *Proceedings of the European conference on computer vision (ECCV)*, pages 801–818, 2018.

[12] Mark Chen, Alec Radford, Rewon Child, Jeffrey Wu, Heewoo Jun, David Luan, and Ilya Sutskever. Generative pretraining from pixels. In *International conference on machine learning*, pages 1691–1703. PMLR, 2020.

[13] Minglin Chen, Yaozu Wu, and Jianhuang Wu. Aggregating multi-scale prediction based on 3d u-net in brain tumor segmentation. In *International MICCAI Brainlesion Workshop*, pages 142–152. Springer, 2019.

[14] Yunpeng Chen, Haoqi Fan, Bing Xu, Zhicheng Yan, Yannis Kalantidis, Marcus Rohrbach, Shuicheng Yan, and Jiashi Feng. Drop an octave: Reducing spatial redundancy in convolutional neural networks with octave convolution. In *Proceedings of the IEEE/CVF International Conference on Computer Vision*, pages 3435–3444, 2019.

[15] Özgün Çiçek, Ahmed Abdulkadir, Soeren S Lienkamp, Thomas Brox, and Olaf Ronneberger. 3d u-net: learning dense volumetric segmentation from sparse annotation. In *International conference on medical image computing and computer-assisted intervention*, pages 424–432. Springer, 2016.

[16] Noel Codella, Veronica Rotemberg, Philipp Tschandl, M Emre Celebi, Stephen Dusza, David Gutman, Brian Helba, Aadi Kalloo, Konstantinos Liopyris, Michael Marchetti, et al. Skin lesion analysis toward melanoma detection 2018: A challenge hosted by the international skin imaging collaboration (isic). *arXiv preprint arXiv:1902.03368*, 2019.

[17] Duwei Dai, Caixia Dong, Songhua Xu, Qingsen Yan, Zongfang Li, Chunyan Zhang, and Nana Luo. Ms red: A novel multi-scale residual encoding and decoding network for skin lesion segmentation. *Medical Image Analysis*, 75:102293, 2022.

[18] Jacob Devlin, Ming-Wei Chang, Kenton Lee, and Kristina Toutanova. Bert: Pre-training of deep bidirectional transformers for language understanding. *arXiv preprint arXiv:1810.04805*, 2018.

[19] Alexey Dosovitskiy, Lucas Beyer, Alexander Kolesnikov, Dirk Weissenborn, Xiaohua Zhai, Thomas Unterthiner, Mostafa Dehghani, Matthias Minderer, Georg Heigold, Sylvain Gelly, et al. An image is worth 16x16 words: Transformers for image recognition at scale. *arXiv preprint arXiv:2010.11929*, 2020.

[20] Alexey Dosovitskiy, Lucas Beyer, Alexander Kolesnikov, Dirk Weissenborn, Xiaohua Zhai, Thomas Unterthiner, Mostafa Dehghani, Matthias Minderer, Georg Heigold, Sylvain Gelly, et al. An image is worth 16x16 words: Transformers for image recognition at scale. *arXiv preprint arXiv:2010.11929*, 2020.

[21] Shuanglang Feng, Heming Zhao, Fei Shi, Xuena Cheng, Meng Wang, Yuhui Ma, Dehui Xiang, Weifang Zhu, and Xinjian Chen. Cpfnet: Context pyramid fusion network for medical image segmentation. *IEEE transactions on medical imaging*, 39(10):3008–3018, 2020.

[22] Markus Frey and Matthias Nau. Memory efficient brain tumor segmentation using an autoencoder-regularized u-net. In *International MICCAI Brainlesion Workshop*, pages 388–396. Springer, 2019.

[23] Peng Gao, Teli Ma, Hongsheng Li, Jifeng Dai, and Yu Qiao. Convmae: Masked convolution meets masked autoencoders. *arXiv preprint arXiv:2205.03892*, 2022.

[24] Fatemeh Haghighi, Mohammad Reza Hosseinzadeh Taher, Michael B Gotway, and Jianming Liang. Dira: Discrimina-

tive, restorative, and adversarial learning for self-supervised medical image analysis. In *Proceedings of the IEEE/CVF Conference on Computer Vision and Pattern Recognition*, pages 20824–20834, 2022.

[25] Ali Hatamizadeh, Yucheng Tang, Vishwesh Nath, Dong Yang, Andriy Myronenko, Bennett Landman, Holger R Roth, and Daguang Xu. Unetr: Transformers for 3d medical image segmentation. In *Proceedings of the IEEE/CVF Winter Conference on Applications of Computer Vision*, pages 574–584, 2022.

[26] Kaiming He, Xinlei Chen, Saining Xie, Yanghao Li, Piotr Dollár, and Ross Girshick. Masked autoencoders are scalable vision learners. In *Proceedings of the IEEE/CVF Conference on Computer Vision and Pattern Recognition*, pages 16000–16009, 2022.

[27] Junjia Huang, Haofeng Li, Guanbin Li, and Xiang Wan. Attentive symmetric autoencoder for brain mri segmentation. In *International Conference on Medical Image Computing and Computer-Assisted Intervention*, pages 203–213. Springer, 2022.

[28] Yuankai Huo, Jiaqi Liu, Zhoubing Xu, Robert L Harrigan, Albert Assad, Richard G Abramson, and Bennett A Landman. Robust multicontrast mri spleen segmentation for splenomegaly using multi-atlas segmentation. *IEEE Transactions on Biomedical Engineering*, 65(2):336–343, 2017.

[29] Liming Jiang, Bo Dai, Wayne Wu, and Chen Change Loy. Focal frequency loss for image reconstruction and synthesis. In *Proceedings of the IEEE/CVF International Conference on Computer Vision*, pages 13919–13929, 2021.

[30] Louise Kauffmann, Stephen Ramanoël, and Carole Peyrin. The neural bases of spatial frequency processing during scene perception. *Frontiers in integrative neuroscience*, 8:37, 2014.

[31] Xiangwen Kong and Xiangyu Zhang. Understanding masked image modeling via learning occlusion invariant feature. *ArXiv*, abs/2208.04164, 2022.

[32] Jiangyun Li, Wenxuan Wang, Chen Chen, Tianxiang Zhang, Sen Zha, Hong Yu, and Jing Wang. Transbtsv2: Wider instead of deeper transformer for medical image segmentation. *arXiv preprint arXiv:2201.12785*, 2022.

[33] Xiangyu Li, Gongning Luo, and Kuanquan Wang. Multistep cascaded networks for brain tumor segmentation. In *International MICCAI Brainlesion Workshop*, pages 163–173. Springer, 2019.

[34] Ze Liu, Yutong Lin, Yue Cao, Han Hu, Yixuan Wei, Zheng Zhang, Stephen Lin, and Baining Guo. Swin transformer: Hierarchical vision transformer using shifted windows. In *Proceedings of the IEEE/CVF International Conference on Computer Vision*, pages 10012–10022, 2021.

[35] Bjoern H Menze, Andras Jakab, Stefan Bauer, Jayashree Kalpathy-Cramer, Keyvan Farahani, Justin Kirby, Yuliya Burren, Nicole Porz, Johannes Slotboom, Roland Wiest, et al. The multimodal brain tumor image segmentation benchmark (brats). *IEEE transactions on medical imaging*, 34(10):1993–2024, 2014.

[36] Fausto Milletari, Nassir Navab, and Seyed-Ahmad Ahmadi. V-net: Fully convolutional neural networks for volumetric medical image segmentation. In *2016 fourth international conference on 3D vision (3DV)*, pages 565–571. IEEE, 2016.

[37] Huu-Giao Nguyen, Celine Fouard, and Jocelyne Troccaz. Segmentation, separation and pose estimation of prostate brachytherapy seeds in ct images. *IEEE Transactions on Biomedical Engineering*, 62(8):2012–2024, 2015.

[38] Henri J Nussbaumer. The fast fourier transform. In *Fast Fourier Transform and Convolution Algorithms*, pages 80–111. Springer, 1981.

[39] Ozan Oktay, Jo Schlemper, Loic Le Folgoc, Matthew Lee, Mattias Heinrich, Kazunari Misawa, Kensaku Mori, Steven McDonagh, Nils Y Hammerla, Bernhard Kainz, et al. Attention u-net: Learning where to look for the pancreas. *arXiv preprint arXiv:1804.03999*, 2018.

[40] Zhiliang Peng, Li Dong, Hangbo Bao, Qixiang Ye, and Furu Wei. Beit v2: Masked image modeling with vector-quantized visual tokenizers. *arXiv preprint arXiv:2208.06366*, 2022.

[41] Yongming Rao, Wenliang Zhao, Zheng Zhu, Jiwen Lu, and Jie Zhou. Global filter networks for image classification. *Advances in Neural Information Processing Systems*, 34:980–993, 2021.

[42] Olaf Ronneberger, Philipp Fischer, and Thomas Brox. U-net: Convolutional networks for biomedical image segmentation. In *International Conference on Medical image computing and computer-assisted intervention*, pages 234–241. Springer, 2015.

[43] Chenyang Si, Weihao Yu, Pan Zhou, Yichen Zhou, Xinchao Wang, and Shuicheng Yan. Inception transformer. *arXiv preprint arXiv:2205.12956*, 2022.

[44] Yucheng Tang, Dong Yang, Wenqi Li, Holger R Roth, Bennett Landman, Daguang Xu, Vishwesh Nath, and Ali Hatamizadeh. Self-supervised pre-training of swin transformers for 3d medical image analysis. In *Proceedings of the IEEE/CVF Conference on Computer Vision and Pattern Recognition*, pages 20730–20740, 2022.

[45] Chenxin Tao, Xizhou Zhu, Gao Huang, Yu Qiao, Xiaogang Wang, and Jifeng Dai. Siamese image modeling for self-supervised vision representation learning. *arXiv preprint arXiv:2206.01204*, 2022.

[46] Philipp Tschandl, Cliff Rosendahl, and Harald Kittler. The ham10000 dataset, a large collection of multi-source dermatoscopic images of common pigmented skin lesions. *Scientific data*, 5(1):1–9, 2018.

[47] Haohan Wang, Xindi Wu, Zeyi Huang, and Eric P Xing. High-frequency component helps explain the generalization of convolutional neural networks. In *Proceedings of the IEEE/CVF Conference on Computer Vision and Pattern Recognition*, pages 8684–8694, 2020.

[48] Wenxuan Wang, Chen Chen, Meng Ding, Hong Yu, Sen Zha, and Jiangyun Li. Transbts: Multimodal brain tumor segmentation using transformer. In *International Conference on Medical Image Computing and Computer-Assisted Intervention*, pages 109–119. Springer, 2021.

[49] Chen Wei, Haoqi Fan, Saining Xie, Chao-Yuan Wu, Alan Yuille, and Christoph Feichtenhofer. Masked feature prediction for self-supervised visual pre-training. In *Proceedings of the IEEE/CVF Conference on Computer Vision and Pattern Recognition*, pages 14668–14678, 2022.

[50] Zhenda Xie, Zheng Zhang, Yue Cao, Yutong Lin, Jianmin Bao, Zhuliang Yao, Qi Dai, and Han Hu. Simmim: A simple framework for masked image modeling. In *Proceedings of the IEEE/CVF Conference on Computer Vision and Pattern Recognition*, pages 9653–9663, 2022.

[51] Hong-Yu Zhou, Chixiang Lu, Chaoqi Chen, Sibei Yang, and Yizhou Yu. A unified visual information preservation framework for self-supervised pre-training in medical image analysis. *IEEE Transactions on Pattern Analysis and Machine Intelligence*, 2023.

[52] Hong-Yu Zhou, Chixiang Lu, Sibei Yang, Xiaoguang Han, and Yizhou Yu. Preservational learning improves self-supervised medical image models by reconstructing diverse contexts. In *Proceedings of the IEEE/CVF International Conference on Computer Vision*, pages 3499–3509, 2021.

[53] Jinghao Zhou, Chen Wei, Huiyu Wang, Wei Shen, Cihang Xie, Alan Yuille, and Tao Kong. ibot: Image bert pre-training with online tokenizer. *arXiv preprint arXiv:2111.07832*, 2021.

[54] Lei Zhou, Huidong Liu, Joseph Bae, Junjun He, Dimitris Samaras, and Prateek Prasanna. Self pre-training with masked autoencoders for medical image analysis. *arXiv preprint arXiv:2203.05573*, 2022.

[55] Man Zhou, Hu Yu, Jie Huang, Feng Zhao, Jinwei Gu, Chen Change Loy, Deyu Meng, and Chongyi Li. Deep fourier up-sampling. *arXiv preprint arXiv:2210.05171*, 2022.

[56] Zongwei Zhou, Md Mahfuzur Rahman Siddiquee, Nima Tajbakhsh, and Jianming Liang. Unet++: A nested u-net architecture for medical image segmentation. In *Deep learning in medical image analysis and multimodal learning for clinical decision support*, pages 3–11. Springer, 2018.